GRAVITATIONAL CONTRACTION OF MAGNETIZED CLOUDS

KOHJI TOMISAKA
Faculty of Education and Human Sciences, Niigata University, 8050 Ikarashi-2, Niigata 950-2181, Japan

Abstract. In this paper, the dynamical contraction of magnetized clouds is studied from the run-away phase to the accretion phase throughout. Since the non-homologous gravitational contraction necessitates progressively finer spatial resolution, "nested grid technique" (Burger & Oliger 1984) is adopted. As a result, it is found that outflow driven by toroidal magnetic fields is occurred in the accretion phase, which explains molecular outflows in protostellar objects (see also Tomisaka 1998). In contrast, a rotationally supported disk is formed in a cloud core without magnetic fields.

1. Introduction

Gravitational contraction continues to be a challenging target for numerical astrophysics, since wide dynamic ranges should be treated both in densities and spatial dimensions. Let us consider an isothermal cloud supported against the self-gravity by the thermal pressure, Lorentz force, and centrifugal force. From Virial analyses and numerical studies to follow-up, it is shown that there is a maximum mass above which a cloud is not in equilibrium. Ignoring the effect of thermal pressure and centrifugal force, the maximum (critical) mass is expressed as a function of the magnetic flux threading the cloud Φ as $M_{\rm cr} \simeq 0.13\Phi/G^{1/2} \simeq 10^3 M_\odot \, (B/30\mu{\rm G}) \, (R/2{\rm pc})^2$. The cloud more massive than the critical mass is called "supercritical." If a cloud is born as supercritical, it begins immediately dynamical collapse and contracts in a gravitational free-fall time-scale $\tau_{\rm ff} \simeq (4\pi G\rho)^{-1/2}$. In contrast, the cloud less massive than $M_{\rm cr}$ is called "subcritical." The subcritical clouds are considered to evolve slowly (10 times slower than $\tau_{\rm ff}$ of the cloud) loosing the magnetic flux mainly near the center of the cloud by the ambipolar diffusion. Due to the ambipolar diffusion, even an initially

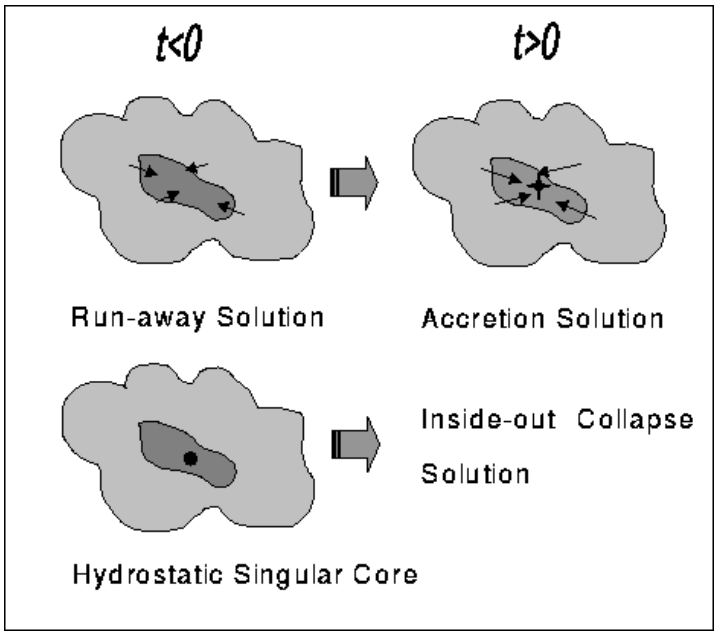

Figure 1. Relationship between run-away collapse solutions and accretion-type solutions realized in isothermal clouds. Dynamical collapse proceeds from the run-away collapse to accretion phase. In particular, when accretion occurs directly in a hydrostatic singular molecular core, the inside-out collapse solution is realized (Shu 1977).

subcritical cloud finally becomes supercritical and experiences dynamical contraction. Therefore, it is concluded that the cloud (core) has to experience the dynamical contraction stage to form stars.

As for a non-magnetic isothermal cloud, semi-analytic (Larson 1969; Penston 1969; Hunter 1977; Whitworth & Summers 1985) and numerical studies (Foster & Chevalier 1993) have revealed that the dynamical collapse of the cloud is divided into two phases: the earlier "run-away collapse" phase and the later "accretion" phase. In the former phase, the cloud shows non-homologous contraction and the central density increases greatly in a finite time scale ($\sim \tau_{\rm ff}$), while in the latter accretion phase the infalling gas accretes onto a central high-density body formed in the run-away collapse phase (Fig. 1). The latter phase corresponds to the "inside-out collapse" (Shu 1977) which is realized when accretion begins at the center of a hydrostatic cloud core. For rotating (non-magnetic) clouds (Norman, Wilson & Barton 1980; Narita, Hayashi & Miyama 1984) and magnetized (non-rotating) clouds (Scott & Black 1980; for recent progress, see Tomisaka 1995), these two phases exist. In this paper, the contraction of magnetized clouds is studied from the run-away phase to the accretion phase through-

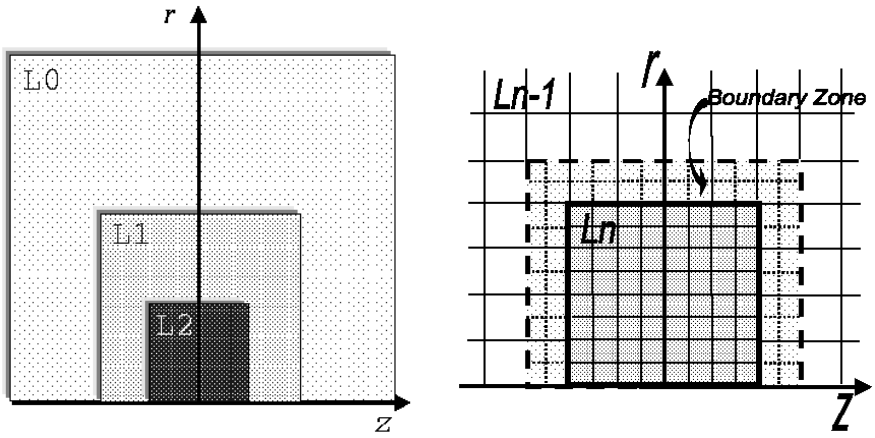

Figure 2. (a) Left: Schematic view of "nested grid method." Each level of grid has a co-center which is identical with the position of the cloud center. (b) Right: Communication between coarser grid L$n-1$ and finer grid Ln. The boundary conditions for Ln (both MHD eqs. and the Poisson eqs.) are given by interpolation of those of L$n-1$. In contrast, in the region covered by Ln, physical values of L$n-1$ are overwritten by averaging over corresponding values of Ln after the calculation of Ln has been completed. Since the Courant condition restricts the time-step, we have to calculate Ln twice and then L$n-1$ once.

out. As a result, it is found that outflow driven by toroidal magnetic fields is occurred in the accretion phase, which explains molecular outflows in protostellar objects (see also Uchida & Shibata 1985; Pudritz & Norman 1986; Ouyed & Pudritz 1997; Shu et al. 1994).

2. Model and Numerical Method

To overcome difficulties related to the wideness of dynamic range, we employ "nested grid method" (Burger & Oliger 1984). A number of grid systems with different spacings are prepared and time evolution is calculated using these grids. Center of the cloud is covered with a finer grid and the global structure is traced by a coarser grid. In this paper, we use 15 levels of grids from L0 (the coarsest) to L14 (the finest). Grid spacing of Ln is chosen as a half of that of L$n-1$ and each level of grids uses 64×64 grid points. Thus, the finest grid (L14's) spacing is $\simeq 10^{-6}$ times smaller than the box size of L0. Since the non-homologous gravitational contraction necessitates progressively finer spatial resolution, the depth of maximum level of grids increases with time. Details of the numerical method are described in separate papers (Tomisaka 1996a,b).

We begin our simulation from an infinitely long, cylindrical, rotating, isothermal cloud in hydrostatic balance, that is, the gravitational force

is counterbalanced with the pressure force, the centrifugal force, and the Lorentz force. Here we assume the rotating axis coincides with the cylinder (z-)axis. As the initial state, only poloidal magnetic fields are taken into account and their strength is assumed proportional to the square root of local gas density. We add small density perturbations on it to initiate contraction. Distributions of density, magnetic flux density, and rotation speed in the radial (r-)direction are taken identical with Matsumoto, Nakamura & Hanawa (1994), although we assume no toroidal magnetic field component B_ϕ initially. The size of the numerical box is chosen to agree with the wavelength of the most unstable mode of the self-gravitational instability $\lambda_{\rm MGR}$ (Matsumoto et al. 1994) and the periodic boundary condition is applied to the upper and lower boundaries in z-direction. Quantities are scaled with the isothermal sound speed c_s, the surface pressure (or surface density) $p_s = c_s^2 \rho_s$ and the corresponding scale-height $H = c_s/(4\pi G \rho_s)^{1/2}$. Typical values would be $c_s = 200{\rm m\ s^{-1}}$, $\rho_s = 100{\rm cm^{-3}}$, $H = 0.36{\rm pc}$, and thus the time-scale is normalized by the free-fall time as $\tau_{\rm ff} = (4\pi G\rho_s)^{-1/2}$ $\simeq 1.75{\rm Myr}(\rho_s/100{\rm cm^{-3}})^{-1/2}$. Using these scalings, initial radial distributions of density, magnetic fields and angular rotation speed are written as

$$\rho(r) = (\rho_c/\rho_s)\{1 + [\rho_c/\rho_s - 2(\Omega_0\tau_{\rm ff})^2]/[8(1+\alpha)] \times (r^2/H^2)\}^{-2}\rho_s, \quad (1)$$

$$(B_z(r), B_r(r)) = ([2\alpha\rho(r)/\rho_s]^{1/2}, 0)\rho_s^{1/2} c_s, \quad (2)$$

$$\Omega(r) = \Omega_0[\rho(r)/\rho_c]^{1/4}. \quad (3)$$

As model parameters, α (the ratio of magnetic pressure to the thermal one for poloidal field component) and Ω_0 (the angular rotation speed at the center of the cloud) are chosen as $\alpha = 0.5$, $\Omega_0 = 5/\tau_{\rm ff}$ and $\rho_c = 100\rho_s$ in the present paper.

3. Results

3.1. RUN-AWAY COLLAPSE PHASE

The evolution is similar to that of magnetized cloud with no rotation (Tomisaka 1995, 1996a; Nakamura, Hanawa, & Nakano 1995). First, the cylindrical cloud breaks into prolate spheroidal fragments which is elongated along the cylinder axis (z-axis). As long as the amplitude of density perturbation is small $\delta\rho/\rho \sim 1$, the shape keeps essentially identical with the most unstable eigen-function of the gravitational instability. Next, gas begins to fall mainly along the magnetic field lines, and forms a disk which runs perpendicular to the magnetic field lines. At $t = 0.5908\tau_{\rm ff}$, at that time the central density ρ_c reaches as high as $10^5\rho_s$ (as the initial density we assume ρ_c is equal to $100\rho_s$), a shock wave is formed parallel to the disk

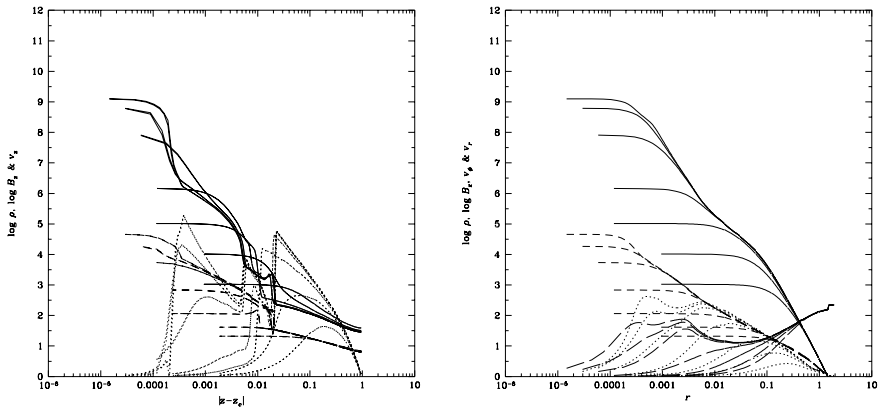

Figure 3. (a) Left: structure along the z-axis. $\log\rho(z, r=0)$ (solid lines), $|v_z(z, r=0)|$ (dotted lines), and $\log B_z(z, r=0)$ (short-dash lines) are plotted. Snapshots are made at $t = 0.5233\tau_{\rm ff}$ ($\rho_c \sim 10^3\rho_s$), $t = 0.5725\tau_{\rm ff}$ ($\rho_c \sim 10^4\rho_s$), $t = 0.5908\tau_{\rm ff}$ ($\rho_c \sim 10^5\rho_s$), $t = 0.5977\tau_{\rm ff}$ ($\rho_c \sim 10^6\rho_s$), $t = 0.5994\tau_{\rm ff}$ ($\rho_c \sim 10^8\rho_s$), $t = 0.5996\tau_{\rm ff}$ ($\rho_c \sim 10^{8.8}\rho_s$), and $t = 0.5997\tau_{\rm ff}$ ($\rho_c \sim 10^{9.1}\rho_s$). (b) Right: structure along the equatorial plane. $\log\rho(z=0, r)$ (solid lines), $|v_r(z=0, r)|$ (dotted lines), $\log B_z(z=0, r)$ (short-dash lines), and $v_\phi(z=0, r)$ (long-dashed lines) are plotted.

(Fig. 3a). It breaks into two waves at the epoch when the central density reaches $\rho_c \sim 10^6\rho_s$: an outer wave front propagates outwardly as a fast-mode MHD shock (seen near $z \sim 0.02H$) and an inner one does inwardly as a slow-mode MHD shock (seen near $z \sim 7 \times 10^{-3}H$) reaching the equator. The rotation angular speed Ω and toroidal magnetic field component B_ϕ also jump crossing the wave fronts. Fast rotation and thus strong B_ϕ are observed in a restricted region between these two fronts. Since the disk contracts in the radial direction, it has a larger Ω than outside the disk. In this configuration, magnetic fields transfers the angular momentum from the disk and redistributes it into the same magnetic flux tube (magnetic braking). However, from this numerical simulation it is shown that the angular momentum is confined into a region inside the fast-mode MHD shock fronts.

Although there exists a number of shock waves ($z \sim 0.02H$, $5 \times 10^{-3}H$, and $2 \times 10^{-4}H$) propagating in the z-direction, no such discontinuity is found in the r-direction (Fig. 3b). However, a kind of modulation is seen around a power-law distribution as $\rho(z=0, r) \propto r^{-2}$, which is related to the formation of multiple shock waves in the z-direction (this is found by Norman et al. (1980) for the case of rotating isothermal cloud). The run-away collapse continues till $t \simeq 0.6\tau_{\rm ff}$ and the central density would increase greatly if the isothermal equation of state continues to be valid. However, when the central density exceeds $10^{10}{\rm cm}^{-3}$, the central part of

the core becomes optically thick for the thermal radiation from dusts and its temperature begins to rise.

3.2. ACCRETION PHASE

In the accretion phase, gas continues to accretes onto the newly formed opaque core. We mimic the situation by using a double polytrope composed of an isothermal one for low density as $p = c_s^2 \rho$ for $\rho < \rho_{\rm crit}$ and a harder one for high density as $p = p(\rho_{\rm crit})(\rho/\rho_{\rm crit})^\Gamma$ for $\rho > \rho_{\rm crit}$. We take $\rho_{\rm crit} = 10^8 \rho_s = 10^{10} {\rm cm}^{-3} (\rho_s / 100 {\rm cm}^{-3})$ and $\Gamma = 5/3$. By virtue of this assumption we can follow further evolution. Figure 4a shows the structure captured by L8 just after the isothermal equation of state is broken. A disk, which runs vertically, contracts radially and gas motion drags and squeezes the magnetic field lines to the center. The rotation speed v_ϕ at that time is not more than the radial infall speed v_r which is in the range of $(2-3) \times c_s$ (see Fig. 3b).

In the accretion phase, the inflow speed is accelerated at least to $(4-5) \times c_s$ and as a result magnetic field lines are strongly dragged and squeezed to the center (see Fig. 1c of Tomisaka 1996b). Beside these, the rotation speed is accelerated as the infall proceeds. Just after the state shown in Figure 1 with the highest central concentration, v_ϕ reaches $\simeq 4 c_s$ at the distance of $r \sim 3 \times 10^{-4} H$ inside of which a nearly spherical core is formed supported mainly by thermal pressure. The rotation velocity v_ϕ exceeds the radial velocity v_r in the accretion phase, while v_ϕ was smaller than v_r (Fig. 3b) in the run-away collapse phase. From this epoch, outflow from the disk is observed.

Figure 4 shows the structures before (a) and after (b) the outflow begins. The physical time scale between (a) and (b) is approximately equal to $\simeq 1000 {\rm yr} (\rho_s / 100 {\rm cm}^{-3})^{-1/2}$. The directions of the magnetic fields in the disk is much affected by the radial inflow. They are pushed and squeezed to the center. It is shown that in the seeding region of the outflow the angle between a magnetic field line and the disk plane decreases from $60^\circ - 70^\circ$ (Fig. 4a) to $10^\circ - 30^\circ$ (Fig. 4b). In Figure 4b, it is indicated that the outflow, which reaches $z_s \sim \pm 0.003 H \simeq \pm 200 {\rm AU} (H/0.36 {\rm pc})$, is confined into two expanding bubbles. In the bubble, the strength of toroidal component of magnetic fields B_ϕ is larger than that of the poloidal one $(B_z^2 + B_r^2)^{1/2}$. Especially at the outer boundary of the bubble $|B_\phi|$ is $(4-5)$ times stronger than $(B_z^2 + B_r^2)^{1/2}$ (see also the upper panel of Fig. 5). Further, the magnetic pressure is much larger than the thermal one. Outside of the bubble, inflow continues.

To see the seeding region of the outflow closely, we plot a close-up view captured by L10 in Figure 5. This figure shows that the outflow is ejected

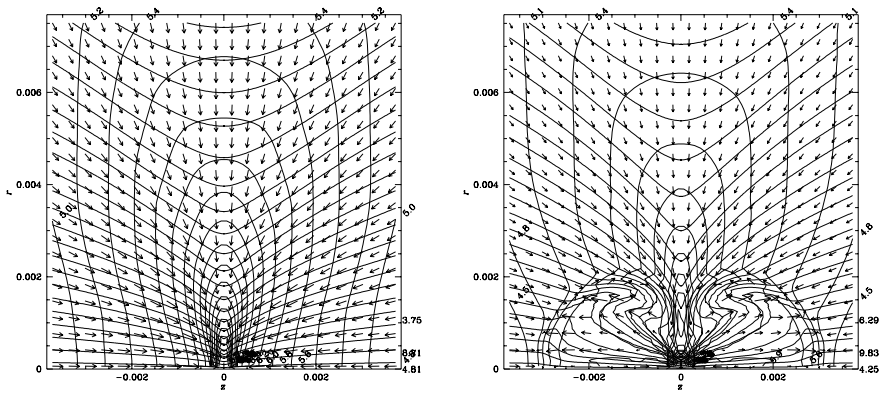

Figure 4. (a) Left: isodensity lines, magnetic field lines, and velocity vectors are plotted for the state when the central density reaches $10^{8.8}\rho_s$ ($t = 0.5996\tau_{\rm ff}$). In contrast to the usual usage, the z-axis is placed horizontally and the r-axis is vertically. (b) Right: the same as (a) but for the state when the central density reaches $10^{10}\rho_s$ ($t = 0.6002\tau_{\rm ff}$). Both are Level 8. Physical time passed between these two is equal to 1000 yr $(\rho_s/100{\rm cm}^{-3})^{-1/2}$.

from the disk near $r \simeq 5 \times 10^{-4} H \simeq 40{\rm AU}(H/0.36{\rm pc})$. This clearly shows that (1) magnetic field lines are almost parallel to the disk surface near the disk. (2) gas inflow in the disk is not disturbed by the outflow from the disk and continues to reach the central core which is supported by the thermal pressure. (3) outflow occurs along magnetic field lines whose inclination angle is in the range of 45° – 60°. This corresponding to the region where $|B_\phi|$ is dominant over the poloidal component (upper panel).

4. Discussion

Inflow and outflow rates are measured at the outer boundary of L10 numerical box as the surface integral of the mass flux density $\int \rho \mathbf{v} \cdot \mathbf{n} dS$. The inflow rate is equal to $2.7 \times 10^2 c_s^3/4\pi G \simeq 4.1 \times 10^{-5} M_\odot {\rm yr}^{-1} (c_s/200{\rm m\ s}^{-1})^3$, which is almost constant in the accretion phase. While, the outflow begins at $t \simeq 0.5998\tau_{\rm ff}$ and the outflow rate increases with time. At the stage shown in Figure 5 it reaches $83 c_s^3/4\pi G \simeq 1.2 \times 10^{-5} M_\odot {\rm yr}^{-1} (c_s/200{\rm m\ s}^{-1})^3$. It is worth notice that the outflow rate attains $\simeq 1/3$ of the inflow rate. The ratio of outflowing mass to inflowing one decreases from L10 to L8.

Linear momentum outflow rate is also measured as the surface integral of the momentum flux density $\int \rho v_z^2 dS$ over the upper and lower boundaries of L10. This increases with time from the epoch of $t \simeq 0.5998\tau_{\rm ff}$ and reaches $\simeq 330 c_s^4/4\pi G \simeq 10^{-5} M_\odot {\rm km\ s}^{-1} {\rm yr}^{-1} (c_s/200{\rm m\ s}^{-1})^4$ at the epoch shown in Figure 5. This is not inconsistent with the momentum outflow rate observed around Class 0 low-mass YSOs from ^{12}CO $J = 2 - 1$ line observations

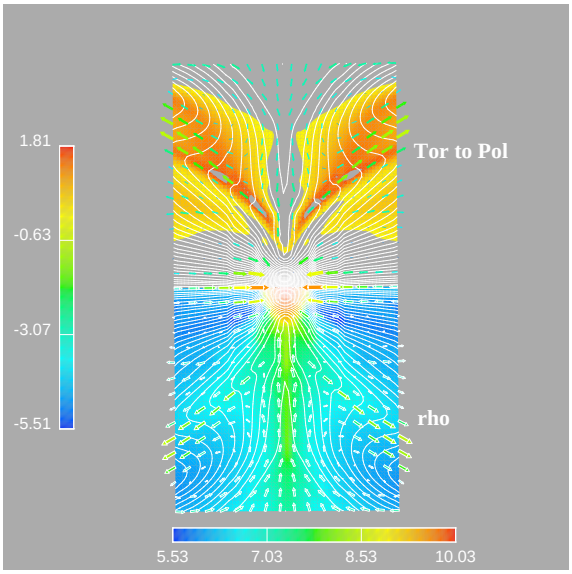

Figure 5. In the lower panel, density distribution (gray scale), magnetic field lines (white line), and velocity fields (vectors) are illustrated. In the upper panel, the ratio of toroidal magnetic pressure $B_\phi^2/8\pi$ to the poloidal one $(B_z^2 + B_r^2)/8\pi$ is plotted as well as the B-fields and velocities. This figure covers $-10^{-3}H \leq z \leq 10^{-3}H$ and $0 \leq r \leq 2 \times 10^{-3}H$, which corresponds to the central 1/16 of the area shown in Fig. 4. Original false color plate is in a supplementary CD-ROM.

(Bontemps et al. 1996) as $3 \times 10^{-6} - 5 \times 10^{-4} M_\odot \mathrm{km\ s^{-1} yr^{-1}}$.

Why does the outflow occur only in the accretion phase? Rotation velocity becomes dominant over the radial velocity only in the accretion phase. This is also indicated in a recent study using a self-similar solution for contracting isothermal rotating disk (Saigo & Hanawa 1998; see their moderately rotating model of $\omega = 0.3$). Further, toroidal magnetic fields develop only in the accretion phase.

This seems to come from the fact that the run-away collapse is fast and as a result the toroidal magnetic fields can not be developed by rotation. In other words, from numerical simulations, the angular rotation speed near the center $\Omega_c(t)$ is proportional to the central free-fall rate as $\Omega_c \simeq (0.2 - 0.4) \times (2\pi G \rho_c)^{1/2}$ (Matsumoto, Hanawa & Nakamura 1997). Therefore, the angle at which a gas element rotates in this free-fall time is as large as $\theta \sim \Omega_c/(2\pi G\rho_c)^{1/2} \sim 0.2 - 0.4$ radian. Since the disk rotates only at $\sim 0.2 - 0.4$ radian, it is concluded that the magnetic field can not be wound much in the run-away collapse phase.

In the accretion phase, we have found a rotating ring nearly in a hydrostatic balance for a model with no magnetic fields ($\alpha = 0$). Since the

angular momentum in the disk is transferred to the outer region by the magnetic effect, a model with poloidal magnetic fields indicates a structure different from the non-magnetic disk. Magnetized disk consists of an innermost nearly hydrostatic core and a rotating disk.

Numerical computations were carried out on VPP300/16R at NAOJ.

References

Bachiller, R. 1996, ARAAp, 34, 111
Basu, S. 1997, ApJ, 485, 240
Bontemps, S., André, P., Terebey, S., & Cabrit, S. 1996, AAp, 311, 858
Burger, M. J., & Oliger, J. 1984, J. Comput. Phys., 53, 484
Foster, P. N., & Chevalier, R. A. 1993, ApJ, 416, 303
Hunter, C. 1977, ApJ, 218, 834
Larson, R. B. 1969, MNRAS, 145, 271
Matsumoto, T., Hanawa, T., & Nakamura, F. 1997, ApJ, 478, 569
Matsumoto, T., Nakamura, F., & Hanawa, T. 1994, PASJ, 46, 243
Nakamura, F., & Hanawa, T. 1997, ApJ, 480, 701
Nakamura, F., Hanawa, T., & Nakano, T. 1995, ApJ, 444, 770
Narita, S., Hayashi, C., & Miyama, S. M. 1984, Prog. Theor. Phys., 72, 1118
Norman, M. L., Wilson, J. R., & Barton, R. T. 1980, ApJ, 239, 968
Ouyed, R., & Pudritz, R. E. 1997, ApJ, 484, 794
Penston, M. V. 1969, MNRAS, 144, 425
Pudritz, R. E., & Norman, C. A. 1986, ApJ, 301, 571
Saigo, K., & Hanawa, T. 1998, ApJ, 493, 342
Scott, E. H., & Black, D. C. 1980, ApJ, 239, 166
Shu, F. H. 1977, ApJ, 214, 488
Shu, F. H., Najita, J., Ostriker, E., Wilkin, F., Ruden, S., & Lizano, S. 1994, ApJ, 429, 781
Tomisaka, K. 1995, ApJ, 438, 226
Tomisaka, K. 1996a, PASJ, 48, 701
Tomisaka, K. 1996b, PASJ, 48, L97
Tomisaka, K. 1998, ApJ, 502, L167
Uchida, Y., & Shibata, K. 1985, PASJ, 37, 515
Whitworth, A., & Summers, D. 1985, MNRAS, 214, 1